JOURNAL OF AIRCRAFT
Vol. 48, No. 4, July–August 2011

Optimal Structural Topology of a Platelike Wing for Subsonic Aeroelastic Stability

Bret Stanford* and Philip Beran†
U.S. Air Force Research Laboratory, Wright-Patterson Air Force Base, Ohio 45433

DOI: 10.2514/1.C031185

This paper discusses the construction of a Pareto tradeoff curve between the flight speed at which a platelike wing encounters an aeroelastic stability and the weight of that wing. The thickness of each finite element is used as a design variable in order to locate the optimal topological reinforcement as a function of the desired location along the Pareto front, as well as the planform of the wing. Three main challenges are addressed. First, the destabilizing flight speed must be located in an accurate and efficient manner. Second, the derivative of the flight speed with respect to a large number of thickness design variables must be computed analytically. Finally, the gradient-based optimization must contend with a discontinuous switch in the critical aeroelastic mode, slowing convergence.

I. Introduction

STRUCTURAL topology optimization (i.e., the distribution of material throughout a design domain) has become a very mature technology over the last 20 years, with substantial contributions to a large number of diverse fields within the design/engineering community [1]. Aeronautical applications, however, are infrequently found in the literature, and aeroelastic studies are rarer still. This research deficiency may be due to the large computational costs typically associated with fluid–structure coupling or, possibly, due to a lack of personnel who are simultaneously interested in the disparate fields of aeroelasticity and topology optimization. Both situations may be expected to improve: the former due to the ever-increasing power of available computer resources, and the latter due to the fact that aeroelasticians are becoming increasingly interested in nontraditional structural layouts and acclimated to novel computational frameworks.

Some recent examples of topology optimization for fluid–structure interactions are given in the work of Maute and Allen [2], Maute and Reich [3], Gomes and Suleman [4], Stanford and Ifju [5], Kobayashi et al. [6], and Yoon [7], with all but the latter specifically concerned with wing design. These papers have all shown an ability to substantially improve the force production and/or efficiency of a flexible wing via prudent use of topology optimization: in some cases, with nonintuitive structural layouts that may not have been arrived at through customary design strategies. As nontraditional aircraft concepts begin to attract considerable attention in the aeroelastic community (joined wing designs, high-altitude long-endurance wings, micro flapping wings, etc. [8]), it is expected that topology optimization can play a substantial role toward effectively tailoring the complex interaction between fluid and structure for optimal performance.

This work is specifically concerned with optimizing the flight speed at which a flexible wing encounters an aeroelastic instability (only flutter and static divergence are considered; the third critical flight speed at which a control surface loses authority is considered by Gomes and Suleman [4]). Several papers exist that attempt to minimize the wing mass under an aeroelastic stability constraint (or some closely related variant) via structural optimization of the thickness distribution of a beam of plate. Examples include Seyranian [9] and Butler and Banerjee [10] (a beam model coupled with strip-theory aerodynamics), Barboni et al. [11], Pastilha [12] (a simply supported panel under supersonic flow modeled via piston theory), and Stroud et al. [13] (a plate model coupled to a doublet-lattice method for reliability-based design). Kameyama and Fukunaga [14] use a similar model to that seen in [13] but study aeroelastic tailoring of swept wings built from composite laminates. Finally, Odaka and Furuya [15] study the stability of a clamped delta wing under supersonic flow modeled via piston theory.

In the majority of these papers, the tradeoff between the critical flight speed at which stability is lost and the mass of the wing is not well understood, as a single optimization is conducted for one metric (e.g., to maximize flutter speed) with a constraint upon the other (e.g., maximum allowable wing mass). Minor changes in the constraint boundary (which is not always known with great certainty) may lead to substantially different optimal designs. It is the goal of this work to construct a Pareto tradeoff curve between the flight speed at which a platelike wing encounters an aeroelastic instability and the weight of that wing. The three-dimensional wing, operating at subsonic flow conditions, is clamped at its root and modeled as a plate. The angle of attack of the wing is zero for the majority of the results presented here, thereby disconnecting the steady-state solution (static aeroelastic deflection) from the flutter speed.

Following the aeroelastic design work of Barboni et al. [11], Stroud et al. [13], and Odaka and Furuya [15], the thickness of each plate element is used as a design variable and allowed to vary continuously between a minimum and a maximum gauge. In this work, techniques are implemented to push each variable toward the boundary as the optimization proceeds, out of practical manufacturing considerations. Conceptually, the optimization problem can be thought of as designing the topology of a stiffening layer (albeit one with the same material properties as the base layer), which may then be interpreted (postprocessed) as spars and ribs. The former idea is discussed by Maute and Allen [2], and the latter is discussed by Kobayashi et al. [6]. The challenges for such an optimization entail first locating the critical flight speed, which may by dynamic (flutter) or static (divergence), computing the derivative of this critical speed with respect to a very large vector of thickness design variables, and finally using these gradients to search the design space in an economical manner. It is expected that, during the search process, the critical speed may switch from one mode to another, providing a discontinuous design space and slowing overall convergence.

II. Analysis Procedures

A. Aeroelastic Equations of Motion

The equations of motion for a platelike wing's unsteady deformation are

Presented as Paper 2010-2841 at the 51st AIAA/ASME/ASCE/AHS/ASC Structures, Structural Dynamics and Materials Conference, Orlando, FL, 12–15 April 2010; received 21 July 2010; revision received 15 November 2010; accepted for publication 17 February 2011.

*National Research Council Postdoctoral Researcher; bret.stanford@wpafb.af.mil.

†Principal Research Aerospace Engineer; philip.beran@wpafb.af.mil. Associate Fellow AIAA.

$$\boldsymbol{M}\cdot\ddot{\boldsymbol{u}}+\boldsymbol{C}\cdot\dot{\boldsymbol{u}}+\boldsymbol{K}\cdot\boldsymbol{u}=\boldsymbol{F} \tag{1}$$

where $\boldsymbol{K}$ is the stiffness matrix computed by discretizing the wing into linear discrete Kirchhoff triangular plate elements (DKT). Each node has three degrees of freedom per node (one out-of-plane translation and two rotations), which are assembled in the solution vector $\boldsymbol{u}$, as well as its time derivatives. $\boldsymbol{M}$ is a consistent mass matrix, $\boldsymbol{C}$ is a viscous damping matrix (given as a linear combination of $\boldsymbol{K}$ and $\boldsymbol{M}$), and $\boldsymbol{F}$ is force vector resulting from aerodynamic loads. To reduce the cost of the system analysis, the solution vector is approximated as a linear combination of a small number of modes:

$$\boldsymbol{u}=\boldsymbol{\Phi}\cdot\boldsymbol{\eta} \tag{2}$$

The modal matrix $\boldsymbol{\Phi}$ contains the modes in each column, and $\boldsymbol{\eta}$ is a vector of modal amplitudes (generalized coordinates). Many choices are available for a reduced basis; as the system of Eq. (1) is linear, natural vibration modes are the obvious choice. Inserting the approximation of Eq. (2) into the equations of motion and premultiplying each term by $\boldsymbol{\Phi}^T$ provides

$$\boldsymbol{\Phi}^T\cdot\boldsymbol{M}\cdot\boldsymbol{\Phi}\cdot\ddot{\boldsymbol{\eta}}+\boldsymbol{\Phi}^T\cdot\boldsymbol{C}\cdot\boldsymbol{\Phi}\cdot\dot{\boldsymbol{\eta}}+\boldsymbol{\Phi}^T\cdot\boldsymbol{K}\cdot\boldsymbol{\Phi}\cdot\boldsymbol{\eta}=\boldsymbol{\Phi}^T\cdot\boldsymbol{F} \tag{3}$$

$$\boldsymbol{M}_r\cdot\ddot{\boldsymbol{\eta}}+\boldsymbol{C}_r\cdot\dot{\boldsymbol{\eta}}+\boldsymbol{K}_r\cdot\boldsymbol{\eta}=\boldsymbol{\Phi}^T\cdot\boldsymbol{F} \tag{4}$$

where the r subscript implies a reduced matrix, each of which is diagonal. Assuming that the wing only deforms out of plane, the wing shape $\boldsymbol{z}$ is the height of each deformed finite element node above the midplane:

$$\boldsymbol{z}=\boldsymbol{z}_o+\boldsymbol{P}\cdot\boldsymbol{u}=\boldsymbol{z}_o+\boldsymbol{P}\cdot\boldsymbol{\Phi}\cdot\boldsymbol{\eta} \tag{5}$$

where $\boldsymbol{z}_o$ is the undeformed wing shape, and $\boldsymbol{P}$ is an interpolation matrix that operates on $\boldsymbol{u}$ (adding in the zero-displacement boundary conditions at the root of the wing and then stripping out the nodal rotations). Similarly, the wing velocity is

$$\dot{\boldsymbol{z}}=\boldsymbol{P}\cdot\dot{\boldsymbol{u}}=\boldsymbol{P}\cdot\boldsymbol{\Phi}\cdot\dot{\boldsymbol{\eta}} \tag{6}$$

The aerodynamic model used in this work is a quasi-steady inviscid vortex lattice method. The wing is discretized into a series of vortex rings, and each spanwise station of the wake is discretized with a single ring that stretches from the trailing edge to the bound vortex (located at some large distance from the wing). A system of equations is built, stipulating that the wing becomes a stream surface of the flow [16]:

$$\boldsymbol{A}(\boldsymbol{z})\cdot\Gamma=\boldsymbol{B}(\boldsymbol{z},\dot{\boldsymbol{z}}) \tag{7}$$

where Γ is the unknown circulation of each ring, and $\boldsymbol{A}$ is an influence matrix: the velocity along the outward normal of the ith control point due to the jth panel. Each member of the matrix is computed as

$$A_{ij}=\{\,u_o\quad v_o\quad w_o\,\}_{ij}\cdot\boldsymbol{n}_i \tag{8}$$

where u_o, v_o, and w_o are the induced velocity (as computed with the Biot–Savart law) by a vortex ring with a unit strength, and $\boldsymbol{n}$ is the outward normal. Although the influence matrix is only a function of the wing geometry $\boldsymbol{z}$, the source vector $\boldsymbol{B}$ depends on the time derivative [Eq. (6)] as well:

$$B_i=-\{\,U\cdot\cos(\alpha)\quad 0\quad U\cdot\sin(\alpha)-\dot{z}_i\,\}\cdot\boldsymbol{n}_i \tag{9}$$

where U is the flight speed, α is the angle of attack, and $\dot{z}_i$ is the deformational velocity of the control point. Equation (7) stipulates that the flow velocity due to wing deformation, flight speed, wake influence, and wing influence must all cancel out along the outward normal of each control point: no penetration. This method differs from a fully unsteady vortex lattice method, where the wake is discretized into a series of panels and the vorticity is periodically shed at each time step, from the trailing edge into the wake [17]. A temporal dependence is added in Eq. (7), however, and so the method has been labeled quasi steady. As will be seen in Sec. IV.A, for the type or problems considered here (i.e., platelike wings of low-to-moderate aspect ratio with low reduced flutter frequencies), the model is adequate.

The aerodynamic force vector $\boldsymbol{F}$ is computed from the circulation of each vortex ring:

$$\boldsymbol{F}=\boldsymbol{Q}\cdot\Gamma \tag{10}$$

where $\boldsymbol{Q}$ is a second interpolation matrix, which converts wing circulation into a differential pressure on each panel and then into a force at each node, and it finally removes the components associated with fixed structural degrees of freedom. The equations of motion are then placed in first-order form:

$$\frac{\mathrm{d}}{\mathrm{d}t}\begin{Bmatrix}\boldsymbol{\eta}\\ \dot{\boldsymbol{\eta}}\end{Bmatrix}=\begin{bmatrix}\boldsymbol{I}&\boldsymbol{0}\\ \boldsymbol{0}&\boldsymbol{M}_r\end{bmatrix}^{-1}\cdot\begin{Bmatrix}\dot{\boldsymbol{\eta}}\\ \boldsymbol{\Phi}^T\cdot\boldsymbol{F}-\boldsymbol{C}_r\cdot\dot{\boldsymbol{\eta}}-\boldsymbol{K}_r\cdot\boldsymbol{\eta}\end{Bmatrix} \tag{11}$$

$$\dot{\boldsymbol{q}}=\boldsymbol{R}(\boldsymbol{q}) \tag{12}$$

where $\boldsymbol{q}$ is a conglomeration of $\boldsymbol{\eta}$ and $\dot{\boldsymbol{\eta}}$, and $\boldsymbol{R}$ is the state-dependent right-hand side. Facilitating both a stability analysis and a sensitivity analysis, the Jacobian is given by

$$\boldsymbol{J}=\frac{\partial\boldsymbol{R}}{\partial\boldsymbol{q}}=\begin{bmatrix}\boldsymbol{I}&\boldsymbol{0}\\ \boldsymbol{0}&\boldsymbol{M}_r\end{bmatrix}^{-1}\cdot\begin{bmatrix}\boldsymbol{0}&\boldsymbol{I}\\ \boldsymbol{\Phi}^T\cdot\frac{\partial\boldsymbol{F}}{\partial\boldsymbol{\eta}}-\boldsymbol{K}_r&\boldsymbol{\Phi}^T\cdot\frac{\partial\boldsymbol{F}}{\partial\dot{\boldsymbol{\eta}}}-\boldsymbol{C}_r\end{bmatrix} \tag{13}$$

The derivative of the force vector with respect to the generalized coordinates $\boldsymbol{\eta}$ is given by the chain rule:

$$\frac{\partial\boldsymbol{F}}{\partial\boldsymbol{\eta}}=\frac{\partial\boldsymbol{F}}{\partial\Gamma}\cdot\frac{\partial\Gamma}{\partial\boldsymbol{z}}\cdot\frac{\partial\boldsymbol{z}}{\partial\boldsymbol{\eta}} \tag{14}$$

The first term on the right of Eq. (14) is $\boldsymbol{Q}$ [Eq. (10)], the third term is $\boldsymbol{P}\cdot\boldsymbol{\Phi}$ [Eq. (5)], and the second term is computed by taking the derivative of Eq. (7) (the vortex lattice method):

$$\frac{\partial\boldsymbol{A}}{\partial\boldsymbol{z}}\cdot\Gamma+\boldsymbol{A}\cdot\frac{\partial\Gamma}{\partial\boldsymbol{z}}=\frac{\partial\boldsymbol{B}}{\partial\boldsymbol{z}} \tag{15}$$

The $\boldsymbol{A}$ and $\boldsymbol{B}$ derivatives are computed by differentiating the Biot–Savart law, as well as the basic geometric relationship used to compute an outward normal [5]. Using these terms, Eq. (14) is rewritten as

$$\frac{\partial\boldsymbol{F}}{\partial\boldsymbol{\eta}}=\boldsymbol{Q}\cdot\boldsymbol{A}^{-1}\left(\frac{\partial\boldsymbol{B}}{\partial\boldsymbol{z}}-\frac{\partial\boldsymbol{A}}{\partial\boldsymbol{z}}\cdot\Gamma\right)\cdot\boldsymbol{P}\cdot\boldsymbol{\Phi} \tag{16}$$

Similarly, the derivative of the force with respect to $\dot{\boldsymbol{\eta}}$ is

$$\frac{\partial\boldsymbol{F}}{\partial\dot{\boldsymbol{\eta}}}=\frac{\partial\boldsymbol{F}}{\partial\Gamma}\cdot\frac{\partial\Gamma}{\partial\dot{\boldsymbol{z}}}\cdot\frac{\partial\dot{\boldsymbol{z}}}{\partial\dot{\boldsymbol{\eta}}} \tag{17}$$

Again, differentiating Eq. (7) (although now, $\boldsymbol{A}$ is not a function of $\dot{\boldsymbol{\eta}}$),

$$\boldsymbol{A}\cdot\frac{\partial\Gamma}{\partial\dot{\boldsymbol{z}}}=\frac{\partial\boldsymbol{B}}{\partial\dot{\boldsymbol{z}}} \tag{18}$$

Finally, the Jacobian can be written as

$$\boldsymbol{J}=\begin{bmatrix}\boldsymbol{I}&\boldsymbol{0}\\ \boldsymbol{0}&\boldsymbol{M}_r\end{bmatrix}^{-1}\begin{bmatrix}\boldsymbol{0}&\boldsymbol{I}\\ \boldsymbol{\Phi}^T\cdot\boldsymbol{Q}\cdot\boldsymbol{A}^{-1}\cdot\left(\frac{\partial\boldsymbol{B}}{\partial\boldsymbol{z}}-\frac{\partial\boldsymbol{A}}{\partial\boldsymbol{z}}\cdot\Gamma\right)\cdot\boldsymbol{P}\cdot\boldsymbol{\Phi}-\boldsymbol{K}_r&\boldsymbol{\Phi}^T\cdot\boldsymbol{Q}\cdot\boldsymbol{A}^{-1}\cdot\frac{\partial\boldsymbol{B}}{\partial\dot{\boldsymbol{z}}}\cdot\boldsymbol{P}\cdot\boldsymbol{\Phi}-\boldsymbol{C}_r\end{bmatrix} \tag{19}$$

B. Location of Critical Speed

Instability of Eq. (12) is found when the real part of any eigenvalue of the Jacobian [Eq. (19)] becomes positive as the flight speed increases. The flutter point in particular is a Hopf bifurcation, where a steady-state solution transitions to an oscillatory solution with a nonzero amplitude [18] (i.e., the real part of the eigenvalue vanishes). Above the flutter point, in the absence of arresting nonlinearities [17], the wing deformation becomes unbounded. There are three general methods for computation of the flutter point. The first entails repeatedly time marching Eq. (12) [or Eq. (4)] out to a steady solution with increasing values of U until an unbounded response is realized. This, however, is very expensive, and the flutter solution is not obtained with a high degree of certainty: the system is very lightly damped (particularly near the flutter speed, where the aerodynamic damping will be zero), and an accurate determination of stability takes many computational time steps.

A second method is to track the eigenvalues of the Jacobian as the speed is gradually increased and note when any one value crosses the real axis [15]. A bisection method can then be used to zoom in and obtain the critical speed with some degree of accuracy. This too can be expensive, as an eigenproblem must be solved repeatedly, particularly if a precise value of the critical speed is needed. The third method solves for the Hopf point in a direct manner at the cost of a steady-state analysis; this technique was introduced by Morton and Beran [18] and extended by Badcock et al. [19] and Woodgate and Badcock [20,21]. The direct method, which is used here, assumes that the speed at which a Hopf bifurcation occurs provides a solution of the form,

$$\boldsymbol{q} = \boldsymbol{q}_e + \varepsilon \cdot (\boldsymbol{q}_1 + i \cdot \boldsymbol{q}_2) \cdot e^{i \cdot \omega \cdot t} \tag{20}$$

where $\boldsymbol{q}_e$ is a steady-state solution (a stationary point), ε is a small parameter, and $(\boldsymbol{q}_1 + i \cdot \boldsymbol{q}_2)$ is the complex eigenvector corresponding to the critical eigenvalue $i \cdot \omega$. Using this form of $\boldsymbol{q}$ in the equations of motion and expanding $\boldsymbol{R}(\boldsymbol{q})$ [from Eq. (12)] in a Taylor series approximation gives

$$\begin{aligned} &\dot{\boldsymbol{q}}_e + \varepsilon \cdot i \cdot \omega \cdot (\boldsymbol{q}_1 + i \cdot \boldsymbol{q}_2) \cdot e^{i \cdot \omega \cdot t} \\ &\quad = \boldsymbol{R}(\boldsymbol{q}_e) + \varepsilon \cdot e^{i \cdot \omega \cdot t} \cdot \boldsymbol{J}(\boldsymbol{q}_e) \cdot (\boldsymbol{q}_1 + i \cdot \boldsymbol{q}_2) + \mathcal{O}(\varepsilon^2) \end{aligned} \tag{21}$$

As $\boldsymbol{q}_e$ is a stationary point, both $\dot{\boldsymbol{q}}_e$ and $\boldsymbol{R}(\boldsymbol{q}_e)$ are zero. Dropping the higher-order terms, Eq. (21) becomes

$$i \cdot \omega \cdot (\boldsymbol{q}_1 + i \cdot \boldsymbol{q}_2) - \boldsymbol{J}_e \cdot (\boldsymbol{q}_1 + i \cdot \boldsymbol{q}_2) = 0 \tag{22}$$

where the Jacobian at the stationary point $\boldsymbol{J}(\boldsymbol{q}_e)$ has been retermed $\boldsymbol{J}_e$. This equation is separated into real and imaginary parts:

$$\boldsymbol{J}_e \cdot \boldsymbol{q}_1 + \omega \cdot \boldsymbol{q}_2 = 0 \qquad \boldsymbol{J}_e \cdot \boldsymbol{q}_2 - \omega \cdot \boldsymbol{q}_1 = 0 \tag{23}$$

A constant array $\boldsymbol{s}$ is used to uniquely define the eigenvector, here defined as the normalized imaginary part:

$$\boldsymbol{s}^T \cdot \boldsymbol{q}_1 = \boldsymbol{s}^T \cdot \boldsymbol{q}_2 - 1 = 0 \tag{24}$$

The Hopf-bifurcation point is finally located by combining Eqs. (23) and (24) into a single system of equations:

$$\boldsymbol{R}_{\mathrm{HB}}(\boldsymbol{Y}) = \begin{Bmatrix} \boldsymbol{J}_e \cdot \boldsymbol{q}_1 + \omega \cdot \boldsymbol{q}_2 \\ \boldsymbol{s}^T \cdot \boldsymbol{q}_1 \\ \boldsymbol{J}_e \cdot \boldsymbol{q}_2 - \omega \cdot \boldsymbol{q}_1 \\ \boldsymbol{s}^T \cdot \boldsymbol{q}_2 - 1 \end{Bmatrix} = 0 \qquad \boldsymbol{Y} = \begin{Bmatrix} \boldsymbol{q}_1 \\ U \\ \boldsymbol{q}_2 \\ \omega \end{Bmatrix} \tag{25}$$

where $\boldsymbol{R}_{\mathrm{HB}}$ is a residual vector and $\boldsymbol{Y}$ is the solution vector composed of the eigenvector, the flow speed U, and the frequency ω. The system is solved with Newton iterations:

$$\boldsymbol{Y}^{n+1} = \boldsymbol{Y}^n - (\boldsymbol{J}_{\mathrm{HB}})^{-1} \cdot \boldsymbol{R}_{\mathrm{HB}} \tag{26}$$

where n is the iteration number. Experience has shown that a good initial guess $\boldsymbol{Y}^0$ is needed to prevent divergence [19] (or convergence to a higher critical speed, or to zero speed, which is also a Hopf-bifurcation point). As such, the aforementioned eigenvalue-tracking bracketing method is used with a relatively large stepping value of ΔU to obtain a very rough estimate for $\boldsymbol{Y}^0$. Then, the direct method [Eq. (26)] is used to locate the precise flutter point (typically converging to machine accuracy within 10 iterations), at which point $U \to U_f$ and $\omega \to \omega_f$ (flutter speed and frequency, respectively).

The Jacobian needed in Eq. (26) is given as

$$\boldsymbol{J}_{\mathrm{HB}} = \begin{bmatrix} \boldsymbol{J}_e & \frac{\partial(\boldsymbol{J}_e \cdot \boldsymbol{q}_1)}{\partial U} & \omega \cdot \boldsymbol{I} & \boldsymbol{q}_2 \\ \boldsymbol{s}^T & \boldsymbol{0} & \boldsymbol{0} & 0 \\ -\omega \cdot \boldsymbol{I} & \frac{\partial(\boldsymbol{J}_e \cdot \boldsymbol{q}_2)}{\partial U} & \boldsymbol{J}_e & -\boldsymbol{q}_1 \\ \boldsymbol{0} & \boldsymbol{0} & \boldsymbol{s}^T & 0 \end{bmatrix} \tag{27}$$

All of the terms in $\boldsymbol{J}_{\mathrm{HB}}$ are known, with the exception of the derivative of the Jacobian terms $\boldsymbol{J}_e \cdot \boldsymbol{q}_1$ and $\boldsymbol{J}_e \cdot \boldsymbol{q}_2$. This term can be ignored, although this will slow down convergence of the Newton iterations [18]. The first term is written as

$$\frac{\partial(\boldsymbol{J}_e \cdot \boldsymbol{q}_1)}{\partial U} = \left(\frac{\partial \boldsymbol{J}_e}{\partial U} + \frac{\partial \boldsymbol{J}_e}{\partial \boldsymbol{q}_e} \cdot \frac{\partial \boldsymbol{q}_e}{\partial U} \right) \cdot \boldsymbol{q}_1 \approx \frac{\partial \boldsymbol{J}_e}{\partial U} \cdot \boldsymbol{q}_1 \tag{28}$$

where $\boldsymbol{J}_e$ shows both explicit dependence and implicit dependence (through the steady-state solution $\boldsymbol{q}_e$) upon the flight speed. The eigenvalue is implicitly dependent upon the speed through $\boldsymbol{q}_e$. Equation (28) would require the derivative of $\boldsymbol{J}_e$ with respect to $\boldsymbol{q}_e$, which would necessitate second derivatives of the vortex lattice method. This is an expensive undertaking, and it is to be avoided: it was found that neglecting the dependence of $\boldsymbol{q}_e$ upon the flight speed is reasonable [in the context of Eq. (28)], resulting in the approximation given on the right of Eq. (28). It should be noted that if the aerodynamic problem is symmetric (i.e., a flat plate at zero angle of attack), $\boldsymbol{q}_e$ becomes trivial and the approximation given in Eq. (28) is exact. The derivative reflecting the explicit dependence of $\boldsymbol{J}_e$ on U is

$$\begin{aligned} \frac{\partial \boldsymbol{J}_e}{\partial U} = \frac{1}{U} \cdot \begin{bmatrix} \boldsymbol{I} & \boldsymbol{0} \\ \boldsymbol{0} & \boldsymbol{M}_r \end{bmatrix}^{-1} \\ \cdot \begin{bmatrix} \boldsymbol{0} & \boldsymbol{0} \\ \boldsymbol{\Phi}^T \cdot \boldsymbol{Q} \cdot \boldsymbol{A}^{-1} \cdot 2 \cdot \left(\frac{\partial \boldsymbol{B}}{\partial z} - \frac{\partial \boldsymbol{A}}{\partial z} \cdot \Gamma \right) \cdot \boldsymbol{P} \cdot \boldsymbol{\Phi} & \boldsymbol{\Phi}^T \cdot \boldsymbol{Q} \cdot \boldsymbol{A}^{-1} \cdot \frac{\partial \boldsymbol{B}}{\partial \dot{z}} \cdot \boldsymbol{P} \cdot \boldsymbol{\Phi} \end{bmatrix} \end{aligned} \tag{29}$$

where it is noted that only $\boldsymbol{Q}$ and $\boldsymbol{B}$ explicitly depend upon the flight speed.

In the event that the divergence speed is lower than the flutter speed, the unstable mechanism is steady. The preceding techniques are all still applicable, although terms associated with unsteady dynamics must be removed. Rather than Eq. (19), the Jacobian is given as

$$\boldsymbol{J} = \boldsymbol{\Phi}^T \cdot \boldsymbol{Q} \cdot \boldsymbol{A}^{-1} \cdot \left(\frac{\partial \boldsymbol{B}}{\partial z} - \frac{\partial \boldsymbol{A}}{\partial z} \cdot \Gamma \right) \cdot \boldsymbol{P} \cdot \boldsymbol{\Phi} - \boldsymbol{K}_r \tag{30}$$

The system of equations needed to locate the divergence point is

$$\boldsymbol{R}_{\mathrm{HB}}(\boldsymbol{Y}) = \begin{Bmatrix} \boldsymbol{J}_e \cdot \boldsymbol{q}_1 \\ \boldsymbol{s}^T \cdot \boldsymbol{q}_1 - 1 \end{Bmatrix} = 0 \qquad \boldsymbol{Y} = \begin{Bmatrix} \boldsymbol{q}_1 \\ U \end{Bmatrix} \tag{31}$$

Upon solution of this nonlinear system of equations (again via Newton iterations), the flight speed $U \to U_d$ (divergence speed). The Jacobian needed for the Newton iterations is

$$\boldsymbol{J}_{\mathrm{HB}} = \begin{bmatrix} \boldsymbol{J}_e & \frac{\partial(\boldsymbol{J}_e \cdot \boldsymbol{q}_1)}{\partial U} \\ \boldsymbol{s}^T & \boldsymbol{0} \end{bmatrix} \tag{32}$$

III. Optimization Procedures

A. Design Derivatives

As noted previously, the design variables for this work are the thickness of each triangular finite element grouped together into the

vector $\boldsymbol{x}$. The number of design variables is expected to be very large ($\sim$1000), and so gradient-based methods are required, necessitating the derivative of either U_f or U_d with respect to $\boldsymbol{x}$, depending on which is lower. It is assumed here that flutter is the critical mechanism, although the approach discussed in this section is equally applicable to divergence. The use of finite differences to compute the derivatives is unadvisable (requiring a costly flutter solution for each design variable), and so an analytical perturbation approach is used here [22]. Assuming that $\boldsymbol{\beta}$ are the eigenvalues of the Jacobian at the flutter speed, then

$$g = \max\{Re[\boldsymbol{\beta}(U_f, \boldsymbol{x})]\} = 0 \tag{33}$$

A perturbation of this relationship at the flutter speed provides

$$\delta g = \frac{\partial g}{\partial U} \cdot \delta U + \frac{\partial g}{\partial \boldsymbol{x}} \cdot \delta \boldsymbol{x} = 0 \tag{34}$$

$$\frac{\partial U_f}{\partial \boldsymbol{x}} = -\left(\frac{\partial g}{\partial U}\right)^{-1} \cdot \frac{\partial g}{\partial \boldsymbol{x}} \tag{35}$$

The desired design derivative thus requires sensitivities of the aerodynamic damping g with respect to both the flutter speed and the structural design variables. Both can be computed from the eigenvalue relationship at the flutter speed:

$$\boldsymbol{J}_e \cdot \boldsymbol{q}_r = \beta \cdot \boldsymbol{q}_r \tag{36}$$

where $\boldsymbol{q}_r$ is the right eigenvector as computed in Eq. (25) ($\boldsymbol{q}_1 + i \cdot \boldsymbol{q}_2$), and β is equal to $i \cdot \omega$. A perturbation of this relationship is given as

$$(\boldsymbol{J}_e + \delta \boldsymbol{J}_e) \cdot (\boldsymbol{q}_r + \delta \boldsymbol{q}_r) = (\beta + \delta\beta) \cdot (\boldsymbol{q}_r + \delta \boldsymbol{q}_r) \tag{37}$$

Dropping higher-order terms, as well as the relationship of Eq. (36), leaves

$$\boldsymbol{J}_e \cdot \delta \boldsymbol{q}_r + \delta \boldsymbol{J}_e \cdot \boldsymbol{q}_r = \beta \cdot \delta \boldsymbol{q}_r + \delta\beta \cdot \boldsymbol{q}_r \tag{38}$$

The left eigenvalue $\boldsymbol{q}_l$ of $\boldsymbol{J}_e$ must then be computed and premultiplied on both sides of Eq. (38). The left-analogous form of Eq. (36) (postmultiplied by $\delta \boldsymbol{q}_r$) then drops from the equality, leaving

$$\boldsymbol{q}_l^T \cdot \delta \boldsymbol{J}_e \cdot \boldsymbol{q}_r = \delta\beta \cdot \boldsymbol{q}_l^T \cdot \boldsymbol{q}_r \tag{39}$$

By dividing both sides of the equation by $\partial \boldsymbol{x}$ and then multiplying through by the inverse of $\boldsymbol{q}_l^T \cdot \boldsymbol{q}_r$, the derivative of the damping with respect to the design variables is finally given as

$$\frac{\partial g}{\partial \boldsymbol{x}} = Re\left(\frac{\partial \beta}{\partial \boldsymbol{x}}\right) = Re\left[(\boldsymbol{q}_l^T \cdot \boldsymbol{q}_r)^{-1} \cdot \left(\boldsymbol{q}_l^T \cdot \frac{\partial \boldsymbol{J}_e}{\partial \boldsymbol{x}} \cdot \boldsymbol{q}_r\right)\right] \tag{40}$$

This expression thus requires the derivative of the Jacobian with respect to each structural design variable. As with Eq. (28), $\boldsymbol{J}_e$ has both an explicit dependence and implicit dependence (through the steady-state solution $\boldsymbol{q}_e$) upon $\boldsymbol{x}$. As before, the dependence of $\boldsymbol{q}_e$ upon $\boldsymbol{x}$ will be neglected: only the explicit relationship is used to compute the derivative, which is exactly true if $\boldsymbol{q}_e$ is a trivial solution. The derivative of Eq. (19) with respect to $\boldsymbol{x}$ is

$$\frac{\partial \boldsymbol{J}_e}{\partial \boldsymbol{x}} = \begin{bmatrix} \boldsymbol{I} & \boldsymbol{0} \\ \boldsymbol{0} & \boldsymbol{M}_r \end{bmatrix}^{-1} \cdot \left(\begin{bmatrix} \boldsymbol{0} & \boldsymbol{0} \\ -\frac{\partial \boldsymbol{K}_r}{\partial \boldsymbol{x}} & -\frac{\boldsymbol{C}_r}{\partial \boldsymbol{x}} \end{bmatrix} - \begin{bmatrix} \boldsymbol{0} & \boldsymbol{0} \\ \boldsymbol{0} & \frac{\partial \boldsymbol{M}_r}{\partial \boldsymbol{x}} \end{bmatrix} \cdot \boldsymbol{J} \right) \tag{41}$$

where only the terms pertaining to the finite element analysis explicitly depend upon the structural design variables rather than the vortex lattice method. The linear mode shapes will explicitly depend upon $\boldsymbol{x}$, although again, this relationship can be neglected for the computation of the reduced matrix derivatives without significant error [23]. For the mass matrix, for example,

$$\frac{\partial \boldsymbol{M}_r}{\partial \boldsymbol{x}} \approx \boldsymbol{\Phi}^T \cdot \frac{\partial \boldsymbol{M}}{\partial \boldsymbol{x}} \cdot \boldsymbol{\Phi} \tag{42}$$

The derivative of $\boldsymbol{M}$ with respect to any member of $\boldsymbol{x}$ is extremely sparse (as each member affects a single finite element) and easy to compute.

The design variable vector $\boldsymbol{x}$ in Eq. (40) can be replaced with U to compute the derivative of the aerodynamic damping with respect to the speed. The required Jacobian derivative has already been computed in Eq. (29). Everything needed for the sought-after critical speed design derivatives in Eq. (35) are then available.

B. Gradient-Based Optimization Details

Structural optimization of aircraft wings typically proceeds by minimizing the weight of the aircraft subjected to critical aeroelastic speed constraints [11] (or vice versa [15]), as well as stress/buckling constraints [13]. However, the structural composition, weight, operable flight speed, critical flight speed, and lift generation of a flexible wing are linked in a complex manner: the adequate selection of constraint boundaries is not always clear, and minor alterations in this boundary can lead to substantially different optimal designs. Computation of the entire Pareto front relating the tradeoff between critical aeroelastic flight speed and the wing weight, although obviously more demanding from an optimization standpoint, can provide a better qualitative understanding of the relationship between the weight and aeroelastic stability. A viable design point can then be selected from the Pareto front based upon considerations not explicitly included in the optimization study.

A weighted-sum approach is taken to compute the Pareto front:

$$\min_{\boldsymbol{x}}\{-w \cdot \min(U_f, U_d) + (1 - w) \cdot V\} \tag{43}$$

such that

$$\begin{cases} x_{\min} < x_i < x_{\max} \\ \max\{Re[\boldsymbol{\beta}(\boldsymbol{x})]\} = 0 \end{cases}$$

where each thickness design variable x_i is bounded by specified side constraints: V is the volume fraction of the wing (as computed from the thickness distribution), and w is a weighting coefficient. The optimization problem of Eq. (43) is solved many times, varying w from zero (where weight minimization is the only objective) to one (where maximization of the critical aeroelastic flight speed is the only objective) to compute the entire Pareto front. Both objective functions in Eq. (43) are normalized to approximately lie between zero and one.

During the optimization process, the critical aeroelastic instability mechanism is liable to switch (from divergence to flutter, for example, or to a higher-mode flutter [14]). The discontinuous nature of the system response will, of course, slow down convergence to the optimal design, but the divergence speed design derivatives (when divergence is an issue at all, which depends strongly upon the wing's planform shape) were not found to be different enough from the flutter derivatives to prevent convergence. The sudden appearance of a higher-mode flutter, accompanied by a drastic drop in the critical speed during the optimization process (as noted by Odaka and Furuya [15]), did not occur in the current work. The reasons behind this are discussed in Sec. IV.C.

All optimization studies are run with the Fletcher–Reeves conjugate gradient algorithm. The design gradients provided to the optimizer naturally push the majority of the thickness variables toward the side constraints, although intermediate values are noted along spatial boundaries between the two limits toward the end of the search process [1]. To push each variable to the side constraint and form well-defined boundaries along the wing, an explicit penalty is added to the objective function of Eq. (43) once the process has converged:

$$X \cdot \sum_{i=1}^{N_{\text{DV}}} \sin\left(\pi \cdot \frac{x_i - x_{\min}}{x_{\max} - x_{\min}}\right) \tag{44}$$

The penalty X is introduced as a small number compared with the objectives given in Eq. (43), and slowly increased from one

optimization iteration to the next. The method has been shown [5] to produce a "0–1" binary design while preserving the qualitative features of the wing topology before the introduction of the penalty, and it similarly succeeds here as well.

IV. Results

A. Model Validation

The aeroelastic model used here is first compared against numerical and experimental results of Attar and Dowell [17], who studied a Lucite delta wing, partially clamped along the root, in subsonic flow conditions. The model used in that work is very similar to that used here, with the exception that their vortex lattice method was truly unsteady (vorticity is periodically shed at each time step from the trailing edge into the discretized wake), as opposed to the quasi-steady assumption used here. Further geometric, structural, and flow parameters can be found in [17]. The first three eigenvalues of the aeroelastic Jacobian are given in Fig. 1 as a function of the flow speed at an angle of attack of zero. A suitable agreement exists between the two aeroelastic frameworks, indicating that the quasi-steady assumption that was made is reasonable. The uncoupled natural frequencies ($U = 0$ m/s) of the delta wing are very close, as are the flutter parameters. The current model predicts a flutter speed of 41.1 m/s and a flutter frequency of 71.1 rad/s, whereas the model used in [17] predicts values of 42.5 m/s and 73.8 rad/s, and experimental testing in [17] measures values of 47.1 m/s and 69.1 rad/s.

The reduced flutter frequency is presumably the metric that indicates a transition from quasi steady to fully unsteady flow features: for the case given in Fig. 1, this value is approximately 0.33 (based upon the semichord). None of the optimization cases discussed here have a reduced flutter frequency greater than 0.36, which may indicate that a quasi-steady aerodynamic model is a reasonable design tool for this work. Even in the event of some bias offset (as previously noted, a quasi-steady flutter speed of 41.1 m/s and an unsteady speed of 42.5 m/s), the gradients can still be very useful, leading the design process in a beneficial direction. As such, many of the design trends discussed next follow well-known strategies for aeroelastic flutter and divergence alleviation; each is highlighted in the related discussion. Finally, it should be noted that the quasi-steady aerodynamic assumption is well founded in the design of wings and panels under flutter constraints; see [11,15,24].

B. Problem Definition

The remainder of the results given in this paper pertain to a flat aluminum wing with a root chord of 0.3 m, clamped along the entirety of the root at an angle of attack of zero. No structural damping is considered (i.e., $\boldsymbol{C}$ is zero), as opposed to the results given in Fig. 1. The taper ratio is fixed at unity, although a variety of wing spans (between 0.6 and 1.8 m) and wing sweeps (between −20 and 20°) are considered, as summarized in Fig. 2. Each wing is assumed to be clamped at the root, and symmetry is assumed across this boundary. The baseline thickness distribution is a uniform value of 1 mm; during the optimization process, the thickness of each finite element is allowed to vary between 0.5 and 1.5 mm. Ten structural modes were found to produce a well-converged reduced-order model, with a flutter speed to within 0.1% of that predicted by the full-order model [Eq. (1)], for the baseline design with a span of 0.6 m.

C. Optimization Convergence Characteristics

Considering, for now, case A (rectangular wing with an aspect ratio of two, as seen in Fig. 2, where the aspect ratio is based upon the full span of 0.6 m), the first four aeroelastic eigenvalues are given in Fig. 3 as a function of flight speed for both a baseline and an optimal wing structure. As noted in the previous section, the baseline wing has a uniform thickness of 1 mm; the topological details of the optimal design will be discussed in the next section. The torsional branch of the baseline wing flutters at 48.6 m/s followed by a hump-mode behavior, after which the mode restabilizes. This flutter mechanism, as also seen in Fig. 1, corresponds to a coalescence of the first bending and torsional modes [17]. The imaginary portion of the bending mode eigenvalue becomes zero at 64.1 m/s (thereby becoming a static mode), and the real portion becomes positive at a divergence speed of 66.9 m/s, although, of course, the critical speed

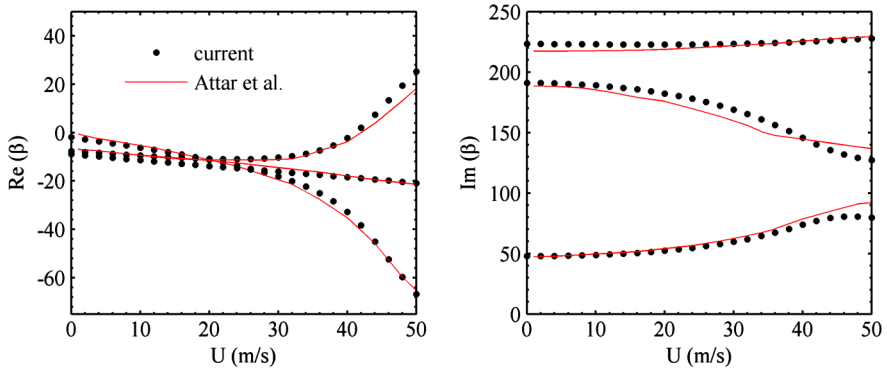

Fig. 1 Aeroelastic eigenvalues as compared with numerical results of Attar and Dowell [17].

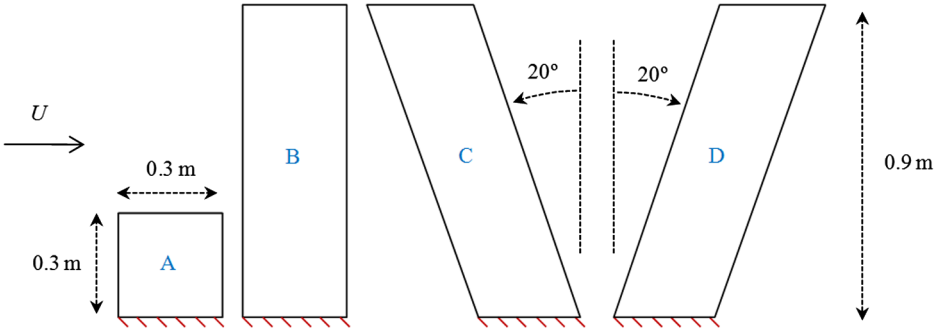

Fig. 2 Four flat-plate wings with a root chord of 0.3, clamped along the root. Flow symmetry is assumed across the clamped boundary.

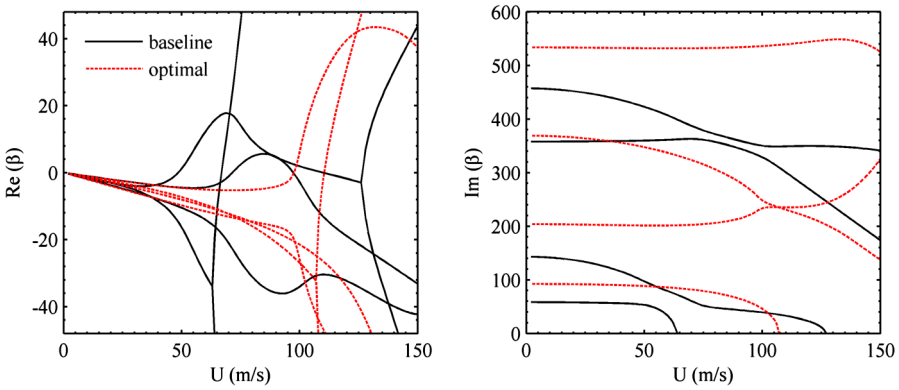

Fig. 3 Aeroelastic eigenvalues of baseline and optimal topologies for wing A.

for this case is the lower flutter value. As expected, instability of the optimal wing occurs at a much higher flow velocity: the flutter speed is 97.6 m/s and the divergence speed is 110.4 m/s. It can be seen that the destabilizing mechanism is completely different for the optimal case, now caused by a merging of the second and third modes (neither of which can be clearly defined as pure bending or torsion).

Details of the optimization process (that produces the optimal of Fig. 3) at each design iteration are given in Fig. 4. For this case, optimization is carried out with $w = 1$ (i.e., single-objective optimization of the critical flight speed). Flutter and divergence speeds are shown in the left, while a root-locus plot of the aeroelastic eigenvalues at the critical flow condition is given on the right. For the baseline design (iteration one), the critical flow speed is flutter, as noted in Fig. 3. As such, a single eigenvalue lies on the imaginary axis (i.e., zero damping), with an imaginary value (flutter frequency) of 99.2 rad/s. The remainder of the four eigenvalues shown lie to the left of the imaginary axis, and they are therefore stable and noncritical. Within the first 10 optimization iterations, the flutter speed remains critical, the optimizer is able to increase the speed at which it occurs, and the associated critical eigenvalue remains on the imaginary axis, traveling upward (i.e., increasing flutter frequency).

Within these first 10 iterations, the design gradients for divergence speed are similar enough to the flutter gradients (discussed below) to cause the divergence speed to increase as well, although at a slower rate. During this portion of the design process, the imaginary part of the eigenvalue associated with wing bending reaches the real axis (i.e., becomes a static mode) and travels toward the origin of the plot. Once the real part becomes zero, divergence is suddenly the critical flight speed, slightly lower than the flutter speed, and the eigenvalue associated with flutter moves just to the left of the imaginary axis (as this mode is now stable). The optimization now proceeds at a much slower rate, frequently switching between critical flutter and divergence flow speeds, with both values gradually increasing.

After 84 iterations, the improvement in objective function is sufficiently slow (design variable step size less than a specified tolerance), so that the external penalty is introduced [Eq. (44)] in order to push each thickness variable to the side constraints (although the majority of the variables reach these bounds naturally, as the

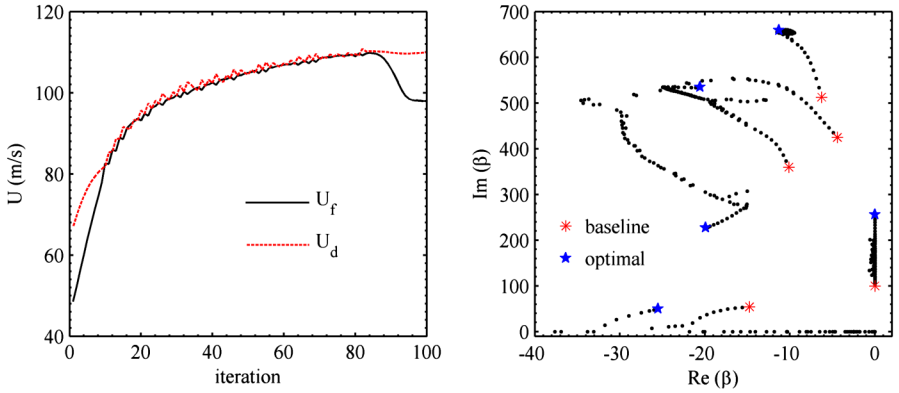

Fig. 4 Critical flow velocity (left) and aeroelastic eigenvalues at critical speed (right) during the optimization process.

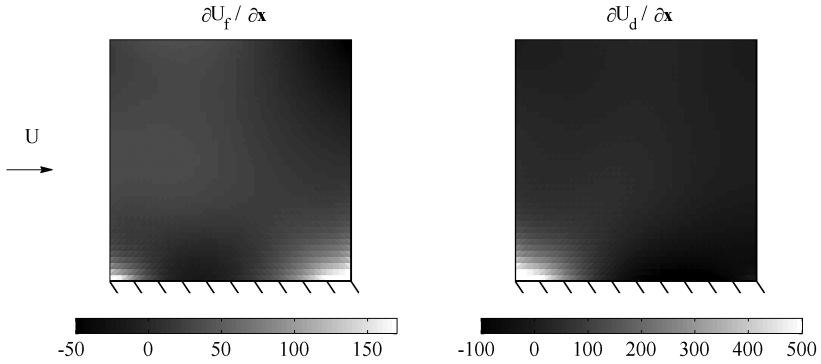

Fig. 5 Derivative of flutter speed (left) and divergence speed (right) with respect to the thickness of each finite element (baseline uniform thickness).

nature of the variable-thickness plate problem shares many similarities with implicit penalization techniques used in compliance-based topology optimization [1]). This strategy decreases the flutter speed to a final value of 97.6; divergence becomes noncritical, and the associated eigenvalue has a large negative real part. During the optimization process, at no point does an eigenvalue travel right of the imaginary axis, and the three higher modes largely become more stable during the process. The advent of higher-mode flutter, a significant issue in the work of Odaka and Furuya [15], is not a problem here, presumably due to the supersonic nature of the flow studied in that work.

The efficiency of the optimization scheme outlined in Eq. (43) is certainly debatable, in light of the muted improvements of the objective function once the flutter and divergence speeds coalesce. An alternative method is the use of frequency separation, which has been used with some success [15]. The method entails finding all of the critical flow velocities above the lowest one (three are shown for the baseline design in Fig. 2, after the flutter speed) and adding a series of constraints that ensure that adjacent critical points are always separated by a buffer. This method can be very expensive, however, as the gradients of each critical point must be computed, and the large number of constraints may be difficult to satisfy. In any case, it is unclear whether such a scheme would be more efficient than the results of Fig. 4, and additional research is required.

Of course, the method seen in Fig. 4 is effective only because the design strategies needed to improve the flutter speed and the divergence speed share similarities. The derivative of the critical speeds with respect to the thickness of each triangular finite element is given in Fig. 5 for the baseline design (a uniform thickness of 1 mm). As expected, the majority of the gradients are positive; additional stiffness (especially when located along the root, where sensitivities are very high) will typically improve aeroelastic stability. Both critical speeds are increased with additional thickness at the leading edge of the root and thinner elements along the midchord of the root, although design trends at the trailing edge of the root differ significantly. Gradients are smaller closer to the wingtip, with the exception of the negative flutter derivative at the trailing edge, which is presumably a mass-related effect. Similarities between the two gradient fields are substantial enough to allow the optimization process in Fig. 4 to switch between both destabilizing mechanisms while improving both, albeit at a relatively slow rate.

D. Optimal Wing Topologies

The complete Pareto tradeoff curve between aeroelastic stability and wing volume fraction is given in Fig. 6 for case A. For this case, the wing is discretized into 3200 triangular elements (a structured 40×40 grid, with each square element divided into two triangles), with each representing a design variable. Volume fraction, which is part of the composite objective function in Eq. (43), varies between zero (a uniform thickness at the lower bound of 0.5 mm) and unity (uniform thickness at the upper bound of 1.5 mm). A series of optimization runs are carried out with increasing values of w [Eq. (43)] from zero to one; the latter case is a single-objective maximization of the critical speed (explicitly seen in Fig. 4). For case A, flutter is the critical destabilizing mechanism along the entire Pareto front, although the divergence speed is shown for each design as well. The actual topologies and their corresponding volume fractions are shown above the graph in Fig. 6 for selected members of the front, where the white and black regions indicate a thickness value at the lower and upper bounds, respectively. Finally, data from aeroelastic plates with uniform thicknesses are given as well, where the plate with a volume fraction of 0.5 represents the baseline design discussed in Figs. 3 and 4. It should be noted that optimizing with a weighting factor w of zero will produce a uniform plate at the lower bound on thickness ($V = 0$), a trivial design. Increasing w to one will not necessarily produce a volume fraction of unity, however, as the flutter and divergence speeds will benefit from having some finite elements reside at the lower bound on thickness.

The expected tradeoff exists between stability and wing mass, with lighter structures necessitating a drop in the critical flight speed, which is always flutter for case A. The relationship between stability and mass is nearly linear for the uniform plates, which are all dominated in a multiobjective sense by the optimal designs along the Pareto front. The most striking example is the heaviest optimal design, found with w set to unity. No premium on mass minimization is included in this optimization process, but the final volume fraction is 0.814: much lighter than the plate with a uniform thickness of 1.5 mm ($V = 1$) and with a higher flutter speed as well. The divergence speed of each optimal design has a very discontinuous relationship with volume fraction, although of course, this is of secondary importance, as divergence is not the critical destabilization mechanism. The design at a volume fraction of 0.438 has no divergence speed, as the eigenvalue is a hump mode for which the peak lies just to the left of the imaginary axis on a root-locus plot.

Focusing now on the topological details themselves (upper portion of Fig. 6), the heaviest wing structure (when w is unity) looks as would be expected from the gradients shown in Fig. 5, with the exception that the trailing edge of the wingtip is at the maximum thickness gauge, a feature that develops in the latter stages of the optimization. Decreasing the value of w, and thus placing more of a premium on mass minimization, gradually shrinks the size of the features. A single batten structure emanating from the leading edge is seen toward the left of the Pareto front and, finally, nothing more than stiffeners along the leading and trailing edges when the volume fraction is less the 0.05. Checkerboard patterns [1] are seen in various

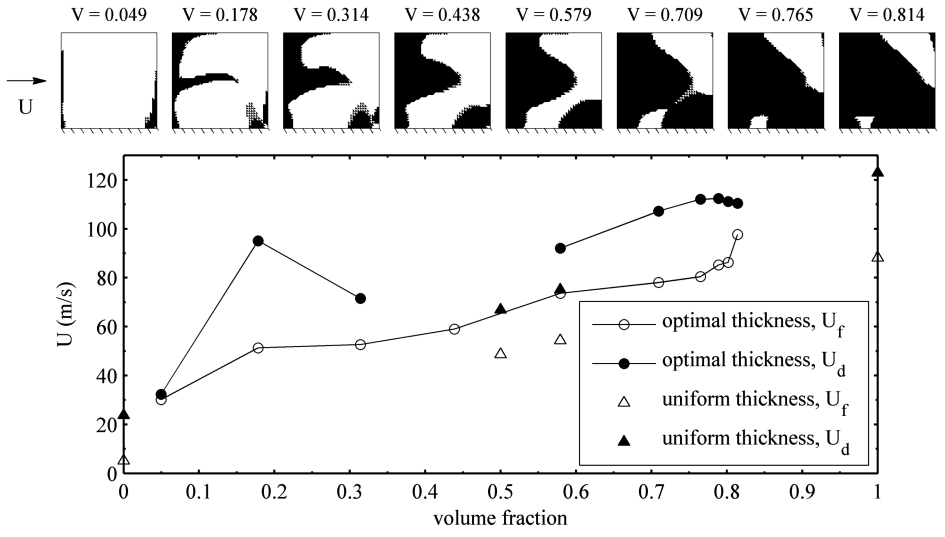

Fig. 6 Optimal wing topologies (top) and weight-stability Pareto front (bottom) for case A.

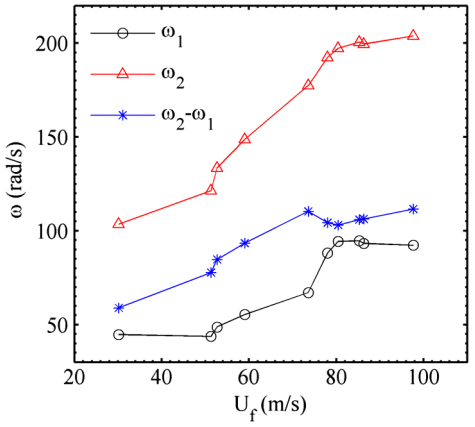

Fig. 7 Uncoupled natural frequencies along the Pareto front for case A.

portions of the wings, largely where the external penalty [Eq. (44)] plays a large role in determining whether an element goes to the minimum or the maximum thickness bound.

A well-known flutter design strategy entails increasing the separation between the first two uncoupled natural frequencies [10,17], which thus delays the coalescence of the first two aeroelastic modes, as seen in Figs. 1 and 3. The topology optimization makes use of this technique as well, as can be seen in Fig. 7, which plots the first two natural frequencies of the Pareto front as a function of the flutter speed for case A. The difference between the two frequencies generally, although not always, leads to an increase in flutter speed. Butler and Banerjee [10] note that simply optimizing this difference is a very suitable surrogate for directly optimizing the flutter speed (and substantially less computationally intensive), although the optimal wing structures are very different. Figure 7 would indicate some success with this technique at the left side of the Pareto front, although potentially less so along the remainder of the front (where the design with a volume fraction of 0.579 has a lower flutter speed but a higher frequency ratio than the remaining designs).

Finally, in order to check the consistency of using Jacobian eigenvalues for stability prediction, as well as emphasize the usefulness of structural stiffness and mass redistribution toward alleviating aeroelastic instabilities without necessarily increasing the wing mass, Eq. (4) is solved via time marching for an optimal design ($U_f = 73.6$ m/s) and a uniform thickness plate ($U_f = 54.3$ m/s). Both have identical volume fractions of 0.579 and an external flow speed of 62 m/s. The initial position and velocity of each modal amplitude is zero, except η_1, which is set to $1.5 \cdot 10^{-4}$. The first three modal amplitudes are shown in Fig. 8: the stable aeroelastic damping is very strong for the optimal design (as the external flow speed is well below the flutter speed), and the system quickly converges to the trivial solution. The opposite is true for the uniform plate, for which the flutter speed is well below the flow speed, leading to a rapid destabilization (negative aeroelastic damping).

The Pareto tradeoff curve between aeroelastic stability and wing volume fraction for case B is given in Fig. 9. A larger number of finite elements are needed to model this higher-aspect ratio wing (a structured 25×75 grid, with each square element divided into two triangles, for a total of 3750 elements), with each being assigned a design variable. The highest critical speed has dropped by a factor of four as compared with the data given in Fig. 6. The flutter speed is still generally critical along both the Pareto front and for the uniform thickness plates but not entirely: the divergence speed is lowest for the optimal design with the volume fraction of 0.365, and the two speeds are nearly identical for the heaviest four members of the front. This area of the Pareto front is very flat, suggesting that little is gained in the way of aeroelastic stability with the increased mass.

The topological details are similar to that seen previously, with a series of batten structures developing at low volume fractions. Frequency-separation strategies, discussed previously, are used here as well, as is mass balancing: a forward shift of the center of gravity [25] to mitigate the onset of flutter. The lightest optimal design ($V = 0.011$) makes use of a lumped mass at the wingtip, which is a simple and well-known tool to separate the bending and torsional frequencies. More interesting, this design does not encounter static divergence before or after the flutter speed, and it is less dominant over the uniform plate with the minimum thickness ($V = 0$) than what was seen in Fig. 6.

A similar tradeoff curve is given in Fig. 10 for case C, which has the same wing span as case B in addition to a 20° forward sweep. This wing geometry couples the elastic motions such that a positive deflection of the wingtip results in a nose-up wing twist, further increasing the loading over the wings [25]. This static load redistribution is obviously a destabilizing influence, and the divergence speed is expected to be the critical flight speed (as opposed to flutter). As can be seen in Fig. 10, for the uniform thickness plates, this is indeed the case, with the divergence speed consistently lower. For the optimal designs along the Pareto front, however, flutter is typically critical, although at the extremes of the front, the two flight speeds are very similar (with divergence being critical for the lightest design). The two heaviest members found via topology optimization are not Pareto optimal: that is, they are dominated by the design with a volume fraction of 0.587, as they have a lower critical flight speed and are heavier. This is almost certainly due to the complex and discontinuous nature of the objective function in this area of the design space. Pareto-optimal designs with the same volume fractions (0.702 and 0.834) presumably exist, but they are difficult to find.

Aeroelastic tailoring via composite laminates has been used to push the divergence speed of forward-swept wings beyond the flight envelope with great success [14,26]. This is done by including the appropriate amount of bend–twist coupling to induce washout and thus stabilize the deformation. Topology optimization can obtain a similar effect, as seen from the wing structures along the upper portion of Fig. 10. A thick structure is oriented diagonally from the leading edge of the wingtip toward the trailing edge, but it is only connected to the clamped root (if at all) by a thin member at the leading edge.

To illustrate the bend–twist coupling of these structures, the static wing deformation is given as a function of flight speed for both an optimal design and a uniform thickness plate with volume fractions

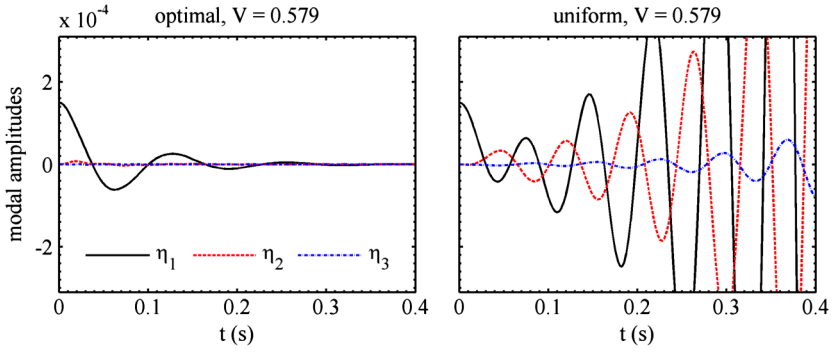

Fig. 8 Vibration of an optimal design (left) and a uniform thickness plate (right) at 62 m/s, case A.

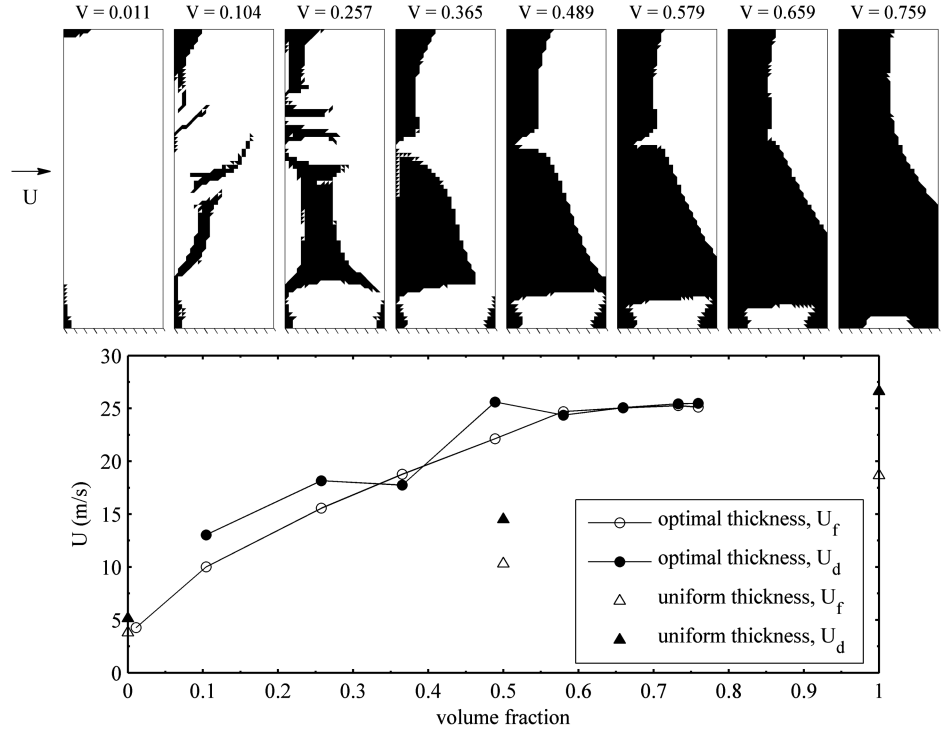

Fig. 9 Optimal wing topologies (top) and weight-stability Pareto front (bottom) for case B.

of 0.437. Both wings are oriented at an angle of attack of 0.1° to the freestream to provide a sufficient disturbance. As expected, an upward deflection of the tip of the uniform wing produces a nose-up twist, both of which become unbounded as the flow velocity approaches the divergence speed. For the optimal design, the tip twist is nearly decoupled from the tip bending, with the topology seen in Fig. 10 successfully counteracting the natural wash-in of the swept wing. At a location closer to the root ($2 \cdot y/b = 0.2$), the coupling is such that the section washes out, stabilizing the loads seen over the wing. The twisting at both sections seen in Fig. 11 is finite, even as the wing diverges due to excessive bending behavior when the velocity approaches its divergence speed (27 m/s).

Finally, the Pareto front between aeroelastic stability and wing volume fraction for the sweptback case D is given in Fig. 12. Contrary to the results given in Fig. 10, backward sweep is naturally stabilizing in a static sense (upward deflection of the wingtip induces a load-alleviating washout at each section [25]); none of the wing structures in Fig. 12 have a divergence speed. Flutter is detrimentally affected by backward sweep, however, but not strongly: flutter speeds for the uniform plates in Fig. 12 are only slightly lower than

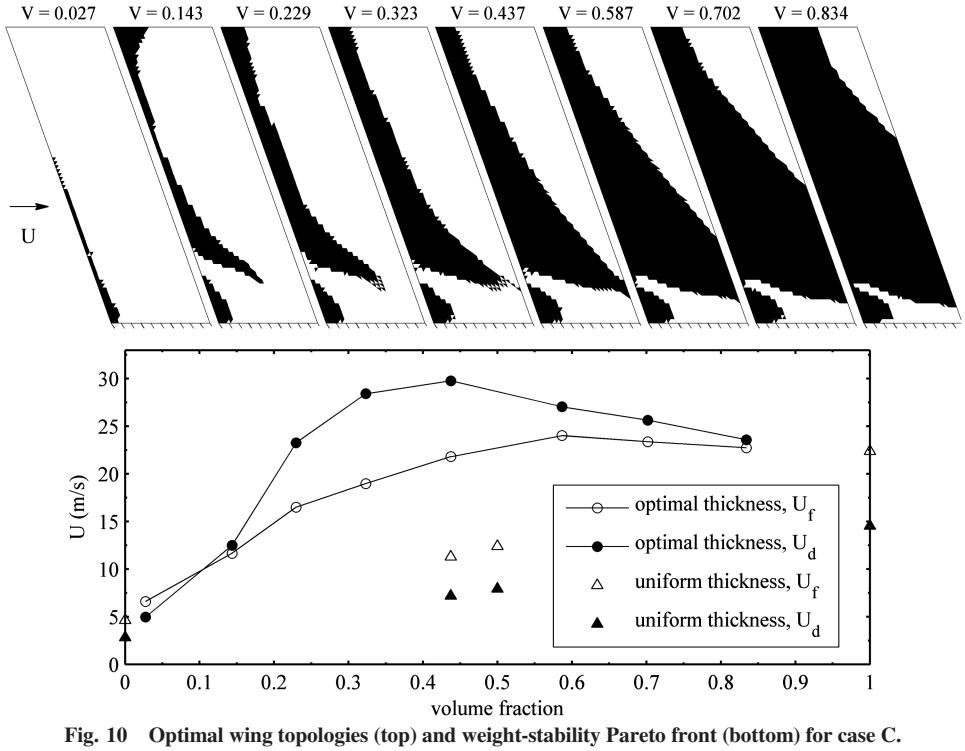

Fig. 10 Optimal wing topologies (top) and weight-stability Pareto front (bottom) for case C.

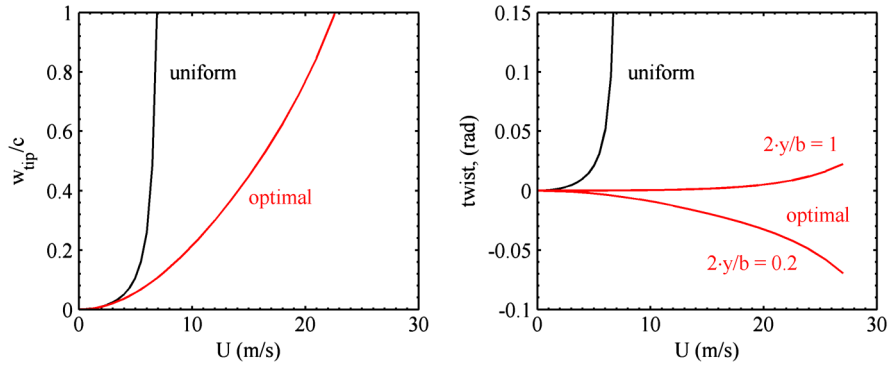

Fig. 11 Static bending/twisting of an optimal design and a uniform thickness plate with volume fractions of 0.437, $\alpha = 0.1°$, case C.

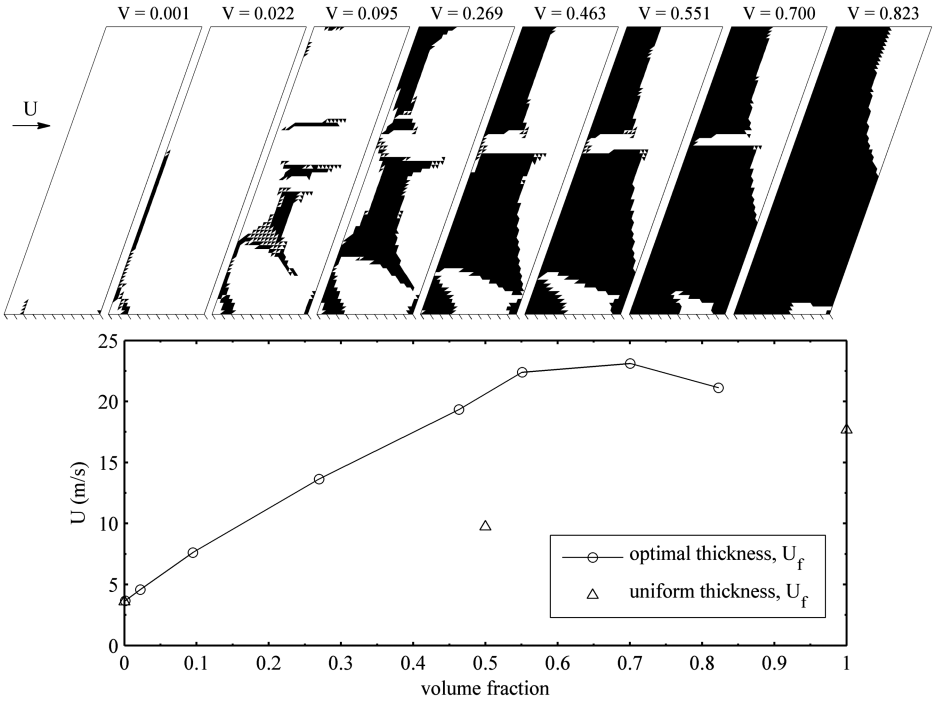

Fig. 12 Optimal wing topologies (top) and weight-stability Pareto front (bottom) for case D.

data in Fig. 9. Furthermore, topological changes throughout the wing along the Pareto front are not significantly different than seen previously for the unswept case, with the exception that the lighter designs do not rely as heavily upon a lumped mass at the wingtip, as was seen in Fig. 9.

V. Conclusions

This paper has detailed efforts toward the use of topology optimization to improve the aeroelastic stability characteristics of platelike wings in subsonic flow. The aeroelastic model consists of a well-validated plate finite element (DKT) coupled with a quasi-steady vortex lattice method. The destabilizing flight speed (either flutter or static divergence) is found by directly solving for the critical eigenvalue of the aeroelastic Jacobian for which the real part becomes zero. The derivative of this critical flight speed is found with respect to the thickness of each finite element via a perturbation technique for use in a gradient-based optimization. The entire Pareto front detailing the tradeoff between critical flight speed and wing mass is computed using a weighted-sum approach for a variety of wing planforms. The following conclusions can be drawn:

1) During the optimization process, the critical flight speed is liable to switch between flutter and divergence (although higher-mode flutter was not observed), providing a moderately discontinuous design space. The design gradients of the two speeds share enough similarities that both can be simultaneously improved, albeit at a slower rate.

2) The use of a variable-thickness topology optimization can consistently locate designs that outproduce uniform thickness plates in a multiobjective sense: higher flutter/divergence speeds, lighter weight.

3) Placing a higher premium on lightweight wing structures decreases the size of the high-thickness topological features, resulting in an array of batten and riblike members.

4) Flutter optimization makes use of well-known design strategies along portions of the Pareto front: namely, separating the first two natural vibration frequencies.

5) The low divergence speed of forward-swept wings is increased via topological reinforcement that induces a washout in response to an upward wing deflection, which counters the natural wash-in of the wing.

Future work will proceed along two branches. First, geometric nonlinearity will be included in the structural plate model in order to examine the effect of a moderate angle of attack upon the flutter and divergence speeds, gradients, and optimal topologies. At speeds above the flutter speed, such a nonlinearity should provide for the formation of limit-cycle oscillations, for which the deterrence may require a disparate topological reinforcement as compared with that

needed for standard flutter optimization. Second, the efficacy of the preceding optimization scheme used will be examined. The discontinuous aeroelastic stability boundary may be effectively traversed with hybrid tools: a combination of gradients based methods and evolutionary schemes.

Acknowledgments

This work is sponsored by the U.S. Air Force Office of Scientific Research under Laboratory Task 03VA01COR (monitored by Fariba Fahroo). The research was performed while the first author held a National Research Council Associateship Award at the U.S. Air Force Research Laboratory.

References

[1] Bendsøe, M., and Sigmund, O., *Topology Optimization*, Springer, Berlin, 2003.

[2] Maute, K., and Allen, M., "Conceptual Design of Aeroelastic Structures by Topology Optimization," *Structural and Multidisciplinary Optimization*, Vol. 27, No. 1, 2004, pp. 27–42. doi:10.1007/s00158-003-0362-z

[3] Maute, K., and Reich, G., "Integrated Multidisciplinary Topology Optimization Approach to Adaptive Wing Design," *Journal of Aircraft*, Vol. 43, No. 1, 2006, pp. 253–263. doi:10.2514/1.12802

[4] Gomes, A., and Suleman, A., "Topology Optimization of a Reinforced Wing Box for Enhanced Roll Maneuvers," *AIAA Journal*, Vol. 46, No. 3, 2008, pp. 548–556. doi:10.2514/1.23028

[5] Stanford, B., and Ifju, P., "Aeroelastic Topology Optimization of Membrane Structures for Micro Air Vehicles," *Structural and Multidisciplinary Optimization*, Vol. 38, No. 3, 2009, pp. 301–316. doi:10.1007/s00158-008-0292-x

[6] Kobayashi, M., Pedro, H., Kolonay, R., and Reich, G., "On a Cellular Division Method for Aircraft Structural Design," *The Aeronautical Journal*, Vol. 113, No. 1150, 2009, pp. 821–831.

[7] Yoon, G., "Topology Optimization for Stationary Fluid–Structure Interaction Problems Using a New Monolithic Formulation," *International Journal for Numerical Methods in Engineering*, Vol. 82, No. 5, 2010, pp. 591–616. doi:10.1002/nme.2777

[8] Livne, E., "Future of Airplane Aeroelasticity," *Journal of Aircraft*, Vol. 40, No. 6, 2003, pp. 1066–1092. doi:10.2514/2.7218

[9] Seyranian, A., "Sensitivity Analysis and Optimization of Aeroelastic Stability," *International Journal of Solids and Structures*, Vol. 18, No. 9, 1982, pp. 791–807. doi:10.1016/0020-7683(82)90036-1

[10] Butler, R., and Banerjee, J., "Optimum Design of Bending-Torsion Coupled Beams with Frequency or Aeroelastic Constraints," *Computers and Structures*, Vol. 60, No. 5, 1996, pp. 715–724. doi:10.1016/0045-7949(95)00451-3

[11] Barboni, R., Mannini, A., and Gaudenzi, P., "On the Use of the P-TFE Method for Panel Flutter Optimization," *Computers and Structures*, Vol. 70, No. 1, 1999, pp. 109–117. doi:10.1016/S0045-7949(98)00180-1

[12] Pastilha, P., "Structural Optimization for Flutter Instability Problems," M.S. Thesis, Technical Univ. of Lisbon, Mechanical Engineering Department, Lisbon, 2007.

[13] Stroud, W., Krishnamurthy, T., Mason, B., Smith, S., Naser, A., "Probabilistic Design of a Plate-Like Wing to Meet Flutter and Strength Requirements," AIAA Structures, Structural Dynamics, and Materials Conference, Denver, CO, AIAA Paper 2002-1464, April 2002.

[14] Kameyama, M., and Fukunaga, H., "Optimum Design of Composite Plate Wings for Aeroelastic Characteristics Using Lamination Parameters," *Computers and Structures*, Vol. 85, No. 3, 2007, pp. 213–224. doi:10.1016/j.compstruc.2006.08.051

[15] Odaka, Y., and Furuya, H., "Robust Structural Optimization of Plate Wing Corresponding to Bifurcation in Higher Mode Flutter," *Structural and Multidisciplinary Optimization*, Vol. 30, No. 6, 2005, pp. 437–446. doi:10.1007/s00158-005-0538-9

[16] Katz, J., and Plotkin, A., *Low-Speed Aerodynamics*, Cambridge Univ. Press, Cambridge, England, U.K., 2001.

[17] Attar, P., and Dowell, E., Tang, D., "A Theoretical and Experimental Investigation of the Effects of a Steady Angle of Attack on the Nonlinear Flutter of a Delta Wing Plate Model," *Journal of Fluids and Structures*, Vol. 17, No. 2, 2003, pp. 243–259. doi:10.1016/S0889-9746(02)00123-8

[18] Morton, S., and Beran, P., "Hopf-Bifurcation Analysis of Airfoil Flutter at Transonic Speeds," *Journal of Aircraft*, Vol. 36, No. 2, 1999, pp. 421–429. doi:10.2514/2.2447

[19] Badcock, K., Woodgate, M., and Richards, B., "Hopf Bifurcation Calculations for a Symmetric Airfoil in Transonic Flow," *AIAA Journal*, Vol. 42, No. 5, 2004, pp. 883–892. doi:10.2514/1.9584

[20] Woodgate, M., and Badcock, K., "Fast Prediction of Transonic Aeroelastic Stability and Limit Cycles," *AIAA Journal*, Vol. 45, No. 6, 2007, pp. 1370–1381. doi:10.2514/1.25604

[21] Badcock, K., and Woodgate, M., "Bifurcation Prediction of Large-Order Aeroelastic Models," *AIAA Journal*, Vol. 48, No. 6, 2010, pp. 1037–1046. doi:10.2514/1.40961

[22] *ZAERO Theoretical Manual*, ZONA Technology Inc., Scottsdale, AZ, 2008.

[23] Kang, B., Park, G., and Arora, J., "A Review of Optimization of Structures Subjected to Transient Loads," *Structural and Multidisciplinary Optimization*, Vol. 31, No. 2, 2006, pp. 81–95. doi:10.1007/s00158-005-0575-4

[24] Gasbarri, P., Chiwiacowsky, L., and de Campos Velho, H., "A Hybrid Multilevel Approach for Aeroelastic Optimization of Composite Wing-Box," *Structural and Multidisciplinary Optimization*, Vol. 39, No. 6, 2009, pp. 607–624. doi:10.1007/s00158-009-0429-6

[25] Bisplinghoff, R., Ashley, H., and Halfman, R., *Aeroelasticity*, Addison-Wesley, Cambridge, MA, 1955.

[26] Shirk, M., Hertz, T., and Weisshaar, T., "Aeroelastic Tailoring: Theory, Practice, and Promise," *Journal of Aircraft*, Vol. 23, No. 1, 1986, pp. 6–18. doi:10.2514/3.45260